Applied Ocean Research 116 (2021) 102882

Contents lists available at ScienceDirect

Applied Ocean Research

journal homepage: www.elsevier.com/locate/apor

Study on suppressing the vortex-induced vibration of flexible riser in frequency domain

Jixiang Song [a,b], Weimin Chen [a,b,*], Shuangxi Guo [a,b], Dingbang Yan [a,b]

[a] Key Laboratory for Mechanics in Fluid-Solid Coupling Systems, Institute of Mechanics, Chinese Academy of Sciences, Beijing 100190, China
[b] School of Engineering Sciences, University of Chinese Academy of Sciences, Beijing 100049, China

ARTICLE INFO

Keywords:
Flexible riser
Vortex-induced vibration
Active control
Frequency domain

ABSTRACT

Vortex-induced vibration (VIV) may cause severe fatigue damage on deep-sea flexible risers. In many researches on active control of VIV, numerical simulation is widely used because of its suitability for parametric studies and lower cost compared to experiments. However, the existing numerical simulations rarely consider the change of lift during the active control of VIV due to the complexity of the control method. Moreover, the calculation time of numerical simulation is relatively long in the time domain. To solve these problems, the active control proposed in this paper is carried out in the frequency domain. A boundary control method considering the change of lift force is proposed through an active control bending moment is applied to the top of riser. Compared with the experimental and numerical results of the flexible riser model under shear flow, the effectiveness of the proposed method is verified. In addition, the effects of different shear currents and different controlled bending moments on structural fatigue damage are studied. The results demonstrated that the reduction of fatigue damage is smaller when the control bending moment is small. As the control bending moment increases, the reduction of fatigue damage increases. However, when the control bending moment exceeds the critical value, the fatigue damage no longer decreases. From the total power perspective, the control energy and the proportion of energy in the system increase with the growth of the control moment. It is difficult to directly obtain the optimal control bending moment although there is an optimal control bending moment. Trial calculations are used to obtain the optimal control bending moment in this paper. The greater the shear currents, the greater the required control bending moment.

1. Introduction

In engineering, the fatigue damage caused by the vortex-induced vibration of the riser cannot be ignored (Liu et al., 2020, Thorsen et al., 2019). Fatigue damage threatens the safety of the riser (Iranpour et al., 2008, Wu et al., 2012). Reducing the fatigue damage of risers is a critical issue (Ren et al., 2019). Since only two ends of the riser are constrained, and the rest of the riser is under the current load, the boundary control method has been widely concerned in active control (How et al., 2009).

There are many methods of boundary controllers, which are roughly divided into three categories, based on Lyapunov method, classical control method, and adaptive control method. The boundary controller based on the Lyapunov direct method or its improved version was applied to control the riser vibration in the time domain (How et al., 2009, Do and Pan, 2008, Do and Pan, 2009, Ge et al., 2010, Zhao et al., 2017, He et al., 2011, Liu and Guo, 2017). Zhao et al. (2019) combined disturbance rejection control strategy, auxiliary system, and Lyapunov theory, to build a new controller and interference observer to attenuate vibration. Guo et al. (2019) used the Lyapunov function to design a control method for a flexible drilling riser system with variable length, variable tension, variable speed, and restricted boundary output. However, the choice of the Lyapunov function is skillful and empirical. Moreover, the Lyapunov function determines the success and effect of the control.

There are also classical control methods, such as PID, linear quadratic Gaussian (LQG), Linear Quadratic Regulator (LQR), neural network, and backstepping. An auto-tuned PID control algorithm was proposed to suppress vibration of riser (Shaharuddin and Darus, 2012). Zhang and Li (2015) applied LQG controller for active control the axial dynamic stress response of deep-water risers. A active control method by applying neural network in tuning top tension of marine riser was

* Corresponding author.
E-mail address: wmchen@imech.ac.cn (W. Chen).

https://doi.org/10.1016/j.apor.2021.102882
Received 31 March 2021; Received in revised form 30 August 2021; Accepted 11 September 2021
Available online 22 September 2021

studied to examine the effectiveness of VIV suppression (Quen et al., 2016). Liu and Guo (2017) used the observer backstepping method to reconstruct the system state and then designed boundary control to suppress the vibration of the riser system. The system state that could be used for feedback when it was impossible to measure. Ji et al. (2018) studied the vibration control of nonlinear three-dimensional Euler-Bernoulli beams with input magnitude and rate constraints. A boundary control scheme is designed to suppress the vibration of beams by backstepping method with smooth hyperbolic tangent function, and satisfies the input amplitude and rate constraints. Based on the LQR method, Yu and Chen (2019) applied a torque actuator on the top of the riser to control vibration. Pham and Hong (2019) studied the flexible marine riser with varying length under the effects of ocean current. To suppress the lateral vibration of riser, boundary control is developed and implemented. The above classical control method is easy to implement, but its applicability in uncertain environment needs to be verified.

Adaptive control has also begun to be applied in the field of active control. For example, Hasheminejad et al. (2014) used the adaptive fuzzy sliding mode control (AFSMC) scheme to actively suppress the 2D VIV of an elastically mounted circular cylinder in CFD under $Re = 90$ and 100. Tavasoli (2015) proposed a robust and adaptive boundary control design method to stabilize the 2D vibration of the hybrid shaft model. The mixed shaft was represented by a set of partial differential equations which control the shaft vibration and coupled with ordinary differential equations, which can represent the rigid body rotation and dynamic boundary conditions. He and Meng (2018) designed an adaptive boundary control suppression scheme for a flexible string system with input hysteresis. The input hysteresis was formulated as a linear desired input and a “disturbance-like” term, whose unknown bound is then estimated by an adaptive law. He et al. (2019) studied the adaptive inverse control problem of a coupled vessel-riser with input backlash and system uncertainties. By introducing an adaptive inverse dynamics of backlash, the backlash control input was decomposed into a mismatch error and a desired control command, and a new adaptive inverse control method is established, which can eliminate vibration, backlash, and the uncertainty of compensation system. Zhao et al. (2020) proposed a framework of dead time compensation and robust adaptive vibration control for uncertain space flexible riser systems. Although adaptive control can be applied to some uncertain environments, most adaptive controls are difficult to understand and are still in the stage of numerical research.

For more information about active control, readers can read the overviews, such as Hong and Shah (2018). However, as far as the author knows, the designed controller is in the time domain in the above literature.The time domain analysis is influenced by the numerical method. For example, the integration times step needs to be controlled within $(1/50)T_{min}$, where T_{min} is the minimum natural period of all participating modes (Li et al., 2018). As the frequency of participating modes increases, the calculation time increases significantly. Compared with time-domain analysis, in frequency domain analysis, the calculation time is short. Therefore, this paper applies the boundary control method in the frequency domain to control the riser’s VIV under shear flow. The main contribution of this paper is to deduce the control law in frequency domain, and to reduce the calculation time and control complexity by using the control moment of simple sinusoidal vibration to suppress single and multi-mode VIV consider the change of lift during the active control of VIV. The paper is structured as follows. In Section 2, the governing partial differential equation (PDE) of the riser with control bending moment and the simplified lift coefficient is proposed. The dynamic response of risers is computed based on the modal superposition method. Next, the prediction of the VIV method in frequency domain is developed with control bending moment in Section 3. The simulation study is presented in Section 4 to demonstrate the effectiveness of the control. The conclusions are drawn in Section 5.

2. Problem formulation and preliminaries

2.1. Dynamics of the marine riser

Fig. 1 shows a schematic of a riser. The motion equation of the riser can be written as a PDE: (How et al., 2009)

$$EI\frac{\partial^4 y(z,t)}{\partial z^4} - T\frac{\partial^2 y(z,t)}{\partial z^2} + m_z\frac{\partial^2 y(z,t)}{\partial t^2} + c\frac{\partial y(z,t)}{\partial z} = f(z,t) \tag{1}$$

where z denotes the length position of riser. y denotes the transverse displacement of the riser. t denotes the time. EI denotes the bending stiffness, T denotes the top tension. m_z denotes the uniform mass per unit length. c denotes the structural damping coefficient. $f(z,t)$ denotes the transverse force per unit length.

The boundary conditions are:

$$y(0,t) = 0 \tag{2}$$

$$EI\frac{\partial^2 y(0,t)}{\partial z^2} = 0 \tag{3}$$

$$y(L,t) = 0 \tag{4}$$

$$EI\frac{\partial^2 y(L,t)}{\partial z^2} - \tau(t) = 0 \tag{5}$$

where $\tau(t)$ is torque applied to the top of the riser.

The force on the riser can be divided into the in-line drag force $F_D(z,t)$ and the oscillating lift $F_L(z,t)$ (Blevins, 1977, Faltinsen, 1990). In order to simplify the complexity of the algorithm, here we only consider the oscillating lift $F_L(z,t)$.

$$F_L(z,t) = \frac{1}{2}\rho C_L\left(\frac{A}{D},t\right)U^2(z)D\cos(2\pi f_v t + \varphi) \tag{6}$$

where $C_L\left(\frac{A}{D},t\right)$ is the spatially and time-varying lift coefficient. ρ represents the seawater density. $U(z)$ is the velocity of the current at z. A is the displacement of the riser. D is the diameter of riser. φ is the phase angle. f_v the non-dimensional vortex shedding frequency can be expressed as

$$f_v = \frac{S_t U}{D} \tag{7}$$

where S_t is the Strouhal number, usually 0.2.

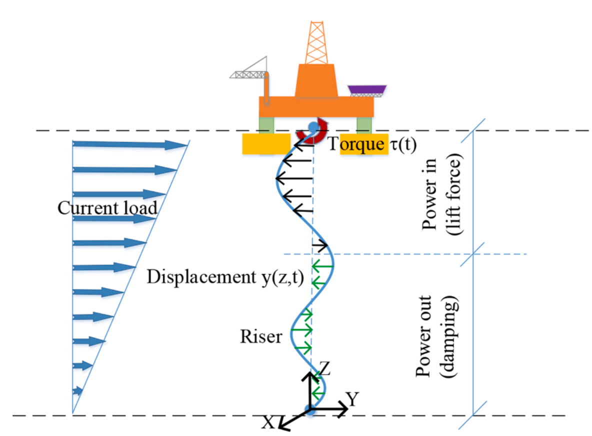

Fig. 1. Schematic of a riser.

2.2. Lift coefficient

The lift coefficient $C_L\left(\frac{A}{D},t\right)$ is affected mainly by the amplitude of the riser, as shown in Fig. 2. Many software (SHEAR7, VIVANA) have empirical lift curves from a large number of experiments. To simplify the complexity of the lift curve, a cubic function is used

$$C_L\left(\frac{A}{D}\right) = C_{L0} + a\left(\frac{A}{D}\right) + b\left(\frac{A}{D}\right)^2 + c\left(\frac{A}{D}\right)^3 \tag{8}$$

where C_{L0} is initial lift coefficient. *a, b, c* are coefficients, respectively. Using the values of the key points (initial value C_{L0}, peak value C_{Lmax}, A_{max}, and zero position A_0) of the original lift curve, a new lift curve can be fitted.

2.3. Dynamic Response

Without considering the external force and damping, Eq. (1) becomes:

$$EI\frac{\partial^4 y(z,t)}{\partial z^4} - T\frac{\partial^2 y(z,t)}{\partial z^2} + m_z\frac{\partial^2 y(z,t)}{\partial t^2} = 0 \tag{9}$$

Based on the mode superposition method, it is assumed that the solution of Eq. (9) is

$$y(z,t) = \sum_{n=1}^{\infty}\psi_n(z)q_n(t) \tag{10}$$

where $\psi_n(z)$ is the shape of vibration, and $q_n(t)$ is the amplitude over time.

The eigenfunction and eigenvalue can be obtained by substituting Eqs. (2), 3, (4), and (10) into Eq. (9),

$$\prod^r = \frac{|Q_r|^2}{2R_r},\ Q_r = \int_{L^r}\frac{1}{2}\rho C_L(z,U_R(z))D(z)U^2(z)\psi_r(z)dz,\ R_r = \int_{L-L^r}R_h(z)\psi_r^2(z)\omega_r dz + \int_0^L R_s(z)\psi_r^2(z)\omega_r dz$$

$$\omega_n = \frac{n\pi}{L}\sqrt{\frac{EI}{m_z}\left(\frac{n\pi}{L}\right)^2 + \frac{T}{m_z}} \tag{11}$$

$$\psi_i(z) = \sqrt{\frac{2}{L}}\left(\sin(\alpha z) - \frac{\sin(\alpha L)}{\sinh(\beta L)}\sinh(\beta z)\right) \tag{12}$$

where $\alpha = \sqrt{\sqrt{\frac{m_z\omega_i}{EI} + \frac{1}{4}\left(\frac{T}{EI}\right)^2} - \frac{1}{2}\left(\frac{T}{EI}\right)^2}$, $\beta = \sqrt{\sqrt{\frac{m_z\omega_i}{EI} + \frac{1}{4}\left(\frac{T}{EI}\right)^2} + \frac{1}{2}\left(\frac{T}{EI}\right)^2}$.

Multiplying each term of Eq. (9) by $\psi_j(z)$ and integrating 0 to L along the Z-direction, we get

$$EI\int_0^L \psi''''_i\psi_j dz - T\int_0^L \psi''_i\psi_j dz - \int_0^L m_z\omega_i^2\psi_i\psi_j dz = 0 \tag{13}$$

The shape of the vibration $\psi_i(z)$ is approximately orthogonal,

$$\int_0^L \psi_i(z)\psi_j(z)dz = \begin{cases}0 & i\neq j\\ 1 & i=j\end{cases} \tag{14}$$

The governing equations of simply supported beams with a moment $\tau(t)$ at the boundary are established based on the principle of virtual work (Weaver et al., 1990).

$$\int_0^L m_z\ddot{y}\delta y dz + \int_0^L (EIy'''' - Ty'')\delta y dz + \int_0^L c\dot{y}\delta y dz = \int_0^L f(z,t)\delta y dz - \tau(t)\delta\left(y'|_{z=L}\right) \tag{15}$$

Variational processing on Eq. (10) gives

$$\delta y(z,t) = \sum_{i=1}^{\infty}\psi_i(z)\delta q_i(t) \tag{16}$$

Substituting Eqs. (13), (14), and (16) into Eq. (15), the Eq. (15) reduces to

$$\sum_{i=1}^{\infty}\left(m_z\ddot{q}_i + c_i\dot{q}_i + m_z\omega_i^2 q_i - \int_0^L f(z,t)\psi_i(z)dz + \tau(t)\psi'_i(L)\right)\delta q_i = 0 \tag{17}$$

where $c_i = 2m_z\omega_i\zeta_i$, $\zeta_i = \zeta_{si} + \zeta_{hi}$, ζ_i is modal damping ratio, ζ_{si} is modal structural damping ratio, ζ_{hi} is modal hydrodynamic damping ratio in section 2.3 Prediction of VIV.

3. Prediction of VIV

According to the method in the SHEAR7 4.4 User Manual (Vandiver and Li, 2005), the VIV is calculated using the new lift curve, the simplified overlap of the power-in regions, and the controlled bending moment. If there is an overlap between adjacent power-in regions, the power-in region length of each mode involved in the overlap shrinks equally until the overlap disappears in SHEAR7. A method is used to reduce the overlap length of each mode by half in this paper.

3.1. Potentially excited modes

$$\prod_R^r = \frac{\prod^r}{\mathrm{Max}\left(\prod_R^i\right)},\ i = 1,2,\cdots,n. \tag{18}$$

where r is r-th mode. n is the total number of modes. $\prod_R^r$ is estimated power ratio for each mode. $\prod^r$ is estimated power for each mode. Q_r is modal force. R_r is modal damping. $R_h(z)$ and $R_s(z)$ are the modal hydrodynamic and structural damping. The L^r is power-in (life force) region. The $L - L^r$ is power-out (hydrodynamic damping) region. The measure of the relative strength of each mode is being sought through

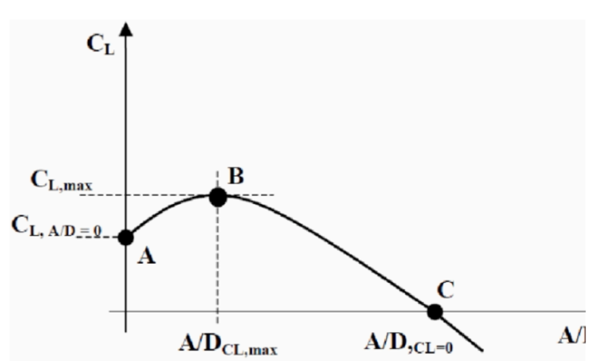

Fig. 2. Typical lift coefficient curve.

Eq. (18).

When the mode is locked, the natural frequency is equal to the shedding frequency of the vortex, i.e., $f_n = f_v$. Substitute Eq. (7) to the formula $U_R(z) = U(z)/(f_n D)$, we get $U_R = 1/S_t$, where U_R is the reduced velocity of current. The bandwidth ΔU_B determines the range of the reduced velocity of current. $U_{nL} = U_R - \frac{1}{2}\Delta U_B U_R$, $U_{nH} = U_R + \frac{1}{2}\Delta U_B U_R$, where U_{nL} is the low reduced velocity of current, U_{nH} is the high low reduced velocity of current. The reduced velocity of current is power-in region in (U_{nL}, U_{nH}), and the power-out region is in the others. So the bandwidth ΔU_B is an important parameter, and usually is defined the following,

$$\Delta U_B = \begin{cases} 0.4 & \text{onemode} \\ 0.2 & \text{severalmodes} \end{cases} \tag{19}$$

3.2. Modal power balance

In the power-in region for mode r, the load force and r-th modal velocity are always in phase. So, the formula for the calculation of the r-th modal force in the r-th mode power-in region is

$$f_r(t) = \int_0^L f(z,t)|\psi_r(z)|dz = \int_{L^r} \frac{1}{2}\rho C_L(z, U_R(z))U^2(z)D\cos(\omega_r t)|\psi_r(z)|dz \tag{20}$$

The modal displacement for mode r is

$$q_r(t) = A_r \sin(\omega_r t) \tag{21}$$

where A_r is the modal displacement amplitude of the structure for mode r.

The modal velocity for mode r is

$$\dot{q}_r(t) = A_r\omega_r\cos(\omega_r t) \tag{22}$$

The r-th modal input power is the r-th modal excitation force $f_r(t)$ times the r-th modal velocity $\dot{q}_r(t)$. The time-average of the modal input power over one period T is

$$\left\langle \prod_r^{in} \right\rangle = \frac{1}{T}\int_0^T \int_{L^r} f_r(t)\dot{q}(t)dzdt = \frac{1}{4}\int_{L^r} \rho D U^2(z) C_L(z, U_R(z)) A_r\omega_r|\psi_r(z)|dz \tag{23}$$

The r-th mode output power is the sum of the rth mode damping force times the r-th mode speed, and the r-th mode bending moment times the r-th mode angular speed. When the phase difference between the bending moment of the r-th mode and the tip angular velocity of the r-th mode is 0, the control effect is optimal. So the r-th mode bending moment is $\tau(t) = -\tau_0\cos(\omega_r t)$.

$$\begin{aligned}\left\langle \prod_r^{out} \right\rangle &= \frac{1}{T}\int_0^T \left(\int_{L-L^r} R_h(z)\psi_r^2(z)A_r^2\omega_r^2\cos^2(\omega_r t)dz + \int_0^L R_s(z)\psi_r^2(z)A_r^2\omega_r^2\cos^2(\omega_r t)dz + \tau(t)\psi'_r(L)A_r\omega_r\cos(\omega_r t) \right)dt \\ &= \frac{1}{2}\left(\int_{L-L^r} R_h(z)\psi_r^2(z)A_r^2\omega_r^2 dz + \int_0^L R_s(z)\psi_r^2(z)A_r^2\omega_r^2 dz + \tau_0\psi'_r(L)A_r\omega_r \right)\end{aligned} \tag{24}$$

It is assumed that, for this mode, input and output power are in balance.

$$\frac{A_r}{D} = \frac{\int_{L^r}\frac{1}{2}\rho C_L(z, U_R(z))U^2(z)|\psi_r(z)|dz}{\int_{L-L^r} R_h(z)\psi_r^2(z)\omega_r dz + \int_0^L R_s(z)\psi_r^2(z)\omega_r dz + \frac{\tau_0}{A_r}\psi'_r(L)} \tag{25}$$

In Eq. (25), the left term represents the dimensionless amplitude of the r-th transverse vortex-induced vibration. Obviously, the smaller the amplitude value, the smaller the stress amplitude and the smaller the fatigue effect. The purpose of control is to reduce the amplitude and resist fatigue. From the right end of Eq. (25), we can see that when the numerator of the fraction is assumed to be fixed, the higher the value of the controlling bending moment in the denominator of the fraction, the smaller the amplitude. According to the analysis of Eq. (25) combined with Fig. 2, when amplitude A/D∈(A_{max}, A_0), lift coefficient distributed on the riser C_L∈(C_{L0}, C_{Lmax}). The control bending moment increases, amplitude A/D decreases, so lift coefficient C_L decreases, and amplitude of the riser A/D decreases greatly. When amplitude A/D $\geq A_{max}$, lift coefficient distributed on the riser $C_L \leq C_{Lmax}$. When control bending moment increases, if amplitude A/D is still greater than A_{max}, so lift coefficient increases, and amplitude A/D reduction is small. If amplitude A/D is less than A_{max}, the lift coefficient decreases, so amplitude decreases greatly. However, the numerator of the fraction is not fixed, because the lift coefficient and the dimensionless vibration amplitude are similar to a convex function, so there will be an optimal solution for controlling the bending moment. However, there is a problem that the excessively applied bending moment will cause fatigue at the applied end, and fatigue after control will be more severe than the fatigue before control. Therefore, the input bending moment needs to be within a reasonable range.

The lift coefficient $C_L\left(\frac{A}{D}, t\right)$ is assigned an initial value. Then, an iteration calculation is started, until convergence is reached (Eq. (25) holds).

Low reduced velocity damping model is:

$$R_h = C_{rl}\rho D U + R_{sw}$$

where C_{rl} is an empirical coefficient. R_{sw} is the still water contribution.

$$R_{sw} = \frac{\omega\pi\rho D^2}{2}\left(\frac{2\sqrt{2}}{\sqrt{\mathrm{Re}_\omega}} + C_{s\omega}\left(\frac{A}{D}\right)^2\right)$$

where $\mathrm{Re}_\omega = \omega D^2/\nu$, ν is the kinematic viscosity of the fluid.

High reduced velocity damping model is:

$$R_h = \frac{C_{rh}\rho U^2}{\omega}$$

where C_{rh} is an empirical coefficient.

The modal damping ratio $\zeta_n = \zeta_h + \zeta_s + \zeta_\tau$.

$$\zeta_h = \frac{\int_{L-L^r} R_h(z)\psi_r^2(z)dz}{2m_z\omega_r}$$

$$\zeta_\tau = \frac{\tau_0}{A_r}\frac{\psi'_r(L)}{2m_z}$$

3.3. A full modal analysis of the structural response

Both the resonant and non-resonant modes are included to get the structural response. From the mode superposition method, we obtain

$$y(z)=\sum_r y(z,\omega_r)=\sum_r\sum_n \psi_r(z)f_{nr}H_{nr}\left(\frac{\omega_r}{\omega_n}\right) \tag{26}$$

where $y(z)$ is the displacement response. f_{nr} is the model force. $H_{nr}\left(\frac{\omega_r}{\omega_n}\right)$ is the frequency response function.

$$f_{nr}=\int_0^L \mathrm{sgn}[\psi_r(z)]\psi_n(z)\frac{1}{2}\rho C_L(z,U_R(z))D(z)U^2(z)dz$$

$$\mathrm{sgn}[\psi_r(z)]=\begin{cases}-1 & \psi_r(z)<0\\ 0 & \psi_r(z)=0\\ 1 & \psi_r(z)>0\end{cases},\ H_{nr}\left(\frac{\omega_r}{\omega_n}\right)=\frac{1}{m_z\omega_n^2}\frac{1}{1-\left(\frac{\omega_r}{\omega_n}\right)^2+j2\zeta_n\frac{\omega_r}{\omega_n}}$$

The commonly used root mean square (RMS) displacement is given by

$$y_{rms}(z)=\left(\sum_r\frac{1}{2}\left|\sum_n\psi_r(z)f_{nr}H_{nr}\left(\frac{\omega_r}{\omega_n}\right)\right|^2\right)^{\frac{1}{2}} \tag{27}$$

The RMS acceleration is given by

$$\ddot{y}_{rms}(z)=\left(\sum_r\frac{1}{2}\omega_r^4\left|\sum_n\psi_r(z)f_{nr}H_{nr}\left(\frac{\omega_r}{\omega_n}\right)\right|^2\right)^{\frac{1}{2}} \tag{28}$$

The input total power is given by

$$\left\langle\prod_{Total}^{in}\right\rangle=\sum_r\left\langle\prod_r^{in}\right\rangle=\frac{1}{4}\sum_r\int_{L^r}\rho DU^2(z)C_L(z,U_R(z))A_r\omega_r|\psi_r(z)|dz \tag{29}$$

The output total power is given by

$$\left\langle\prod_{Total}^{out}\right\rangle=\left\langle\prod_{Total}^{out}\right\rangle_H+\left\langle\prod_{Total}^{out}\right\rangle_S+\left\langle\prod_{Total}^{out}\right\rangle_\tau$$

$$\left\langle\prod_{Total}^{out}\right\rangle_H=\sum_r\left\langle\prod_r^{out}\right\rangle_H=\frac{1}{2}\sum_r\left(\int_{L-L^r}R_h(z)\psi_r^2(z)A_r^2\omega_r^2dz\right)$$

$$\left\langle\prod_{Total}^{out}\right\rangle_S=\sum_r\left\langle\prod_r^{out}\right\rangle_S=\frac{1}{2}\sum_r\left(\int_0^L R_s\psi_r^2(z)A_r^2\omega_r^2dz\right) \tag{30}$$

$$\left\langle\prod_{Total}^{out}\right\rangle_\tau=\sum_r\left\langle\prod_r^{out}\right\rangle_\tau=\frac{1}{2}\sum_r(\tau_0\psi'_r(L)A_r\omega_r)$$

where $\langle\prod_{Total}^{out}\rangle_H$ is the output total power of hydrodynamic force. $\langle\prod_{Total}^{out}\rangle_S$ is the Output total power of structural damping, $\langle\prod_{Total}^{out}\rangle_\tau$ is the control total power.

3.4. Damage rate

The RMS stress at z due to all modes is

$$S_{rms}(z)=\left(\sum_r\frac{1}{8}\left|\sum_n\psi''_nEd_sf_{nr}H_{nr}\left(\frac{\omega_r}{\omega_n}\right)\right|^2\right)^{\frac{1}{2}} \tag{31}$$

Table 1
Mechanical properties of the riser.

Parameters of the physical system	Value
Length of riser(L)	9.63m
Mass per unit length(m_z)	1.013kg/m
Outer diameter(D)	0.02m
Sea water density(ρ)	1024kg/m^3
Structural modal damping ratio(ζ_s)	0.3%
Tension(T)	700N
Flexural rigidity(EI)	135.4 N·m^2

where E is Young's modulus, ψ''_n is the curvature for mode n, and d_s is the strength diameter.

The damage rate at location z due to all modes is given by the summation of the individual modal damage rates.

$$D(z)=\sum_r D_r(z) \tag{32}$$

The damage rate $D_r(z)$ due to excitation frequency ω_r is given by

$$D_r(z)=\frac{\omega_r}{2\pi C}\left(2\sqrt{2}S_{r,rms}(z)\right)^b\Gamma\left(\frac{b+2}{2}\right)$$

$$S_{r,rms}(z)=\frac{1}{2\sqrt{2}}\left|\sum_n\psi''_nEd_sf_{nr}H_{nr}\left(\frac{\omega_r}{\omega_n}\right)\right|$$

$$NS^b=C$$

where b and C are constants, S is the stress amplitude, Γ is the Gamma distribution function.

4. Numeric analysis

To validate the proposed approach, the calculation is performed with the example of VIVDR (Zheng, 2007), namely, Case one. The transverse force is simulated using the oscillating lift $F_L(z,t)$ with initial value C_{L0}=0.3, peak value C_{Lmax}=0.70, when A_{max}=0.3, and zero position A_0=1.1. $S_t=0.18$. And the properties of the riser model are listed in Table 1. The Test1216 Naked_riser Shear V1.54 is chosen to compare. $U(z)$ is a shear current, $U_{Bottom}(0)=0.14m/s$,$U_{Top}(L)=1.54m/s$. $C_{rl}=0.18$, $C_{s\omega}=0.2$, and $C_{rh}=0.2$. The cutoff is 0.1. Fig. 3 (a) and Fig. 3 (b) are the time history of current velocity $U_{Top}(L)$ and the time history of displacement of the riser Z/L=0.44, respectively. The stable segment data of 15 ~ 45 seconds are intercepted from the figure for analysis. It can be seen from Fig. 3 (c) that the displacement prediction results of the present method are close to the experimental results under this condition(U_{Top}=1.533m/s), and the error meets the engineering accuracy.

To validate the proposed approach, the calculation is performed with the example of SHEAR7 (Vandiver, 2012), namely, Case two. The transverse force is simulated using the oscillating lift $F_L(z,t)$ with initial value C_{L0}=0.3, peak value C_{Lmax}=0.70, when A_{max}=0.3, and zero position A_0=1.1. $S_t=0.18$. $U(z)$ is a shear current, $U_{Bottom}(0)=0.3048m/s$,$U_{Top}(L)=0.9144m/s$.$C_{rl}=0.18$, $C_{s\omega}=0.2$, and $C_{rh}=0.2$. The cutoff is 0.1. The first 15 modes are selected here, i.e., n is 15. b=3.74, C=2.45 × 10^{13}. And the properties of the riser model are listed in Table 2.

Comparing with the results of SHEAR7, it is confirmed that the current calculation results are reliable in Figs. 4 (a)–7 (a). The lift coefficients, Non-dimensional RMS displacement, RMS acceleration, and Fatigue damage distributions in SHEAR7 are in general agreement with the values in the proposed approach.

The lift coefficients in SHEAR7, the proposed approach (bending moment input of 0 N·m), bending moment input of 5 N·m, 10 N·m, 15 N·m, 20 N·m, 100 N·m, 1000 N·m, and 10000 N·m are shown in Fig. 4. The 6 modes (modes 9, 10, 11, 12, 13, and 14) involved in the vibration due to the cutoff value (0.1) of the elimination mode. The distribution length of the lift coefficient is obtained from the distribution length of the lift coefficient of the 6 modes by reducing the overlap length of each mode by half. Each mode lift coefficient is applied to the riser with the corresponding modal vibration frequency. To facilitate observation, it is divided into four parts. The lift coefficients decrease as the bending moment input increases. The maximum lift coefficient is from approximately 0.7 to approximately 0.3 when bending moment input from 0 N·m to 100 N·m. The maximum lift coefficient at 100 N·m is close to initial value C_{L0}=0.3. This means that the displacement is close to zero. However, when the bending moment input continues to increase from

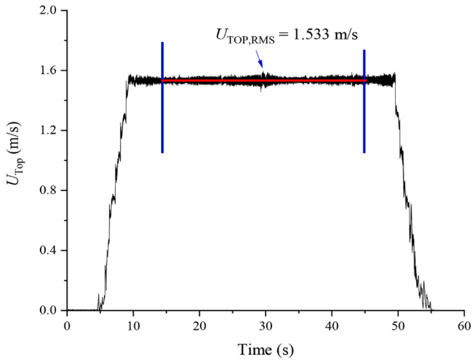

(a) Test1216 Naked_riser Shear V1.54m/s

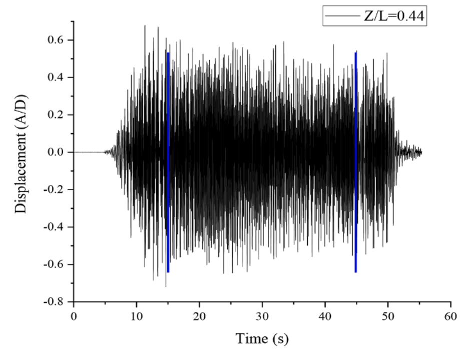

(b)The time history of displacement (A/D) at Z/L=0.44

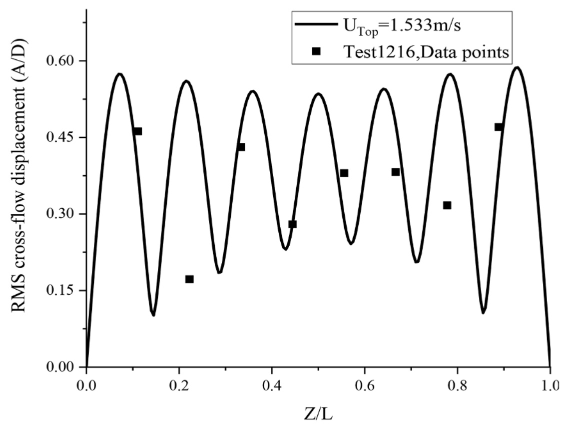

(c) The displacement prediction of the present method and Test1216 Naked_riser Shear V1.54

Fig. 3. The present method and Test1216 Naked_riser Shear V1.54.

Table 2
Mechanical properties of the riser.

Parameters of the physical system	Value
Length of riser(L)	60.96m
Mass per unit length(m_z)	2.0313kg/m
Outer diameter(D)	0.033274m
Sea water density(ρ)	1024kg/m^3
Structural modal damping ratio(ζ_s)	0.3%
Tension(T)	3558.5776N
Flexural rigidity(EI)	425.754 N·m^2
Elastic modulus(E)	1.235×10^{10} N/m^2

100 N·m to 10000 N·m, the lift coefficient increases. This is an interesting phenomenon that deserves our attention. It is further shown that there is an optimal solution for the control moment.

Fig. 5 shows the non-dimensional RMS displacement with and without control bending moment. The displacement decreases as the bending moment input increase from 0 N·m to 100 N·m. The maximum displacement under 0 N·m (0.43, Z/L=0.960) is 8.11 times the maximum displacement under 100 N·m (0.053, Z/L=0.545). The maximum position is from the top to the middle of the riser. Under 100 N·m, 1000 N·m, and 10000 N·m, the displacements almost coincide. It shows that with the increase of the bending moment, the vibration displacement of the riser gradually decreases, approaching the minimum value, but not zero. Because controlling the bending moment only suppress the displacement of dominant mode, but not the displacement of inexcited mode.

Fig. 6 shows the RMS acceleration with and without control bending moment. The acceleration decreases as the bending moment input increase from 0 N·m to 100 N·m. Under 100 N·m, 1000 N·m, and 10000 N·m, the acceleration almost coincides, just like displacement in Fig. 5.

At last, the fatigue damage distributions along riser are studied in Fig. 7. The fatigue damage decreases as the bending moment input increases. Under 20 N·m, 100 N·m, 1000 N·m, and 10000 N·m, the fatigue damage almost coincide. If controlling the minimum bending moment as the optimal condition, obviously 20 N·m is optimal. The maximum fatigue damage of 20 N·m is only 5.09×10^{-4} of the maximum fatigue damage of the uncontrolled riser. It is equivalent to increasing the service life of the riser by 1.966×10^{3} years. It can be seen from Eq. (20) that the theoretical optimal solution is challenging to obtain. So the control bending moment of 20 N·m in this example is not the optimal solution but is relatively closer to the optimal solution than other moments.

From the total power (see Fig. 8), it can be seen that the input total power, output total power of hydrodynamic force and output total power of structural damping decrease as the bending moment from 0 N·m to 100 N·m increase, and increase slightly after bending moment is greater than 100 N·m. The control total power first increases with the increase of the control bending moment from 0 N·m to 10 N·m, decreases when the control bending moment is (10,100) N·m, and increases significantly after bending moment is greater than 100 N·m. There is a maximum value near 10 N·m, which is an interesting phenomenon, because the reduction of displacement increases the lift coefficient, so the control total power increases. There is a minimum value about 100 N·m, which is because the displacement decreases close to 0, the lift coefficient is close to C_{L0}, so the control total power is the smallest. From the total power ratio (see Fig. 9), it can be seen that the control energy

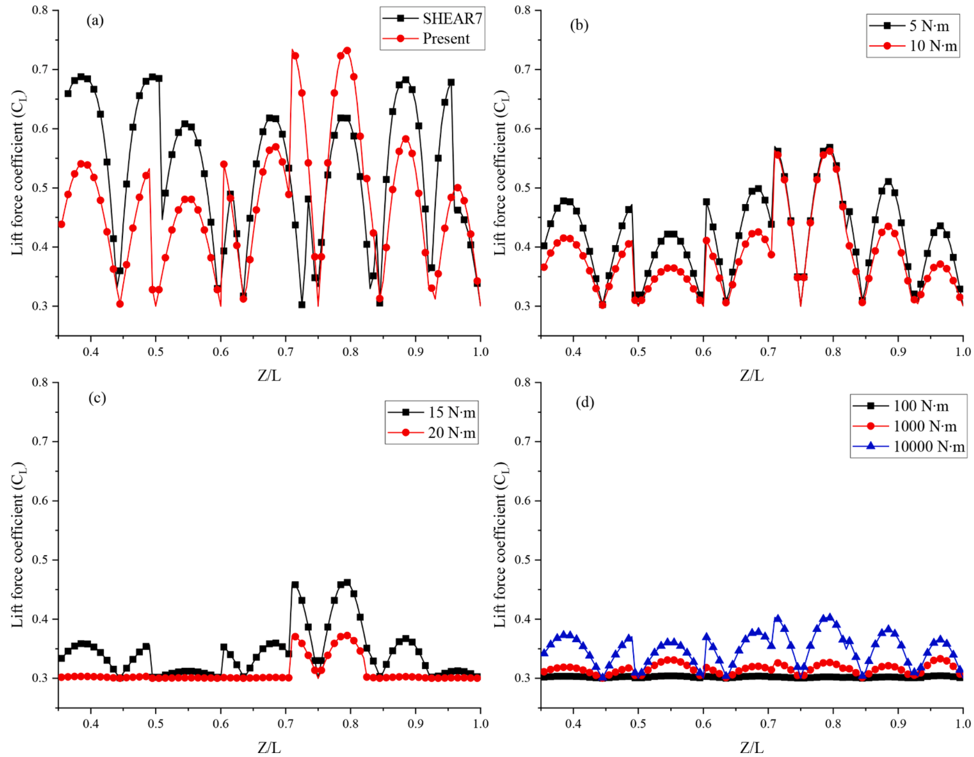

Fig. 4. Lift force coefficient.

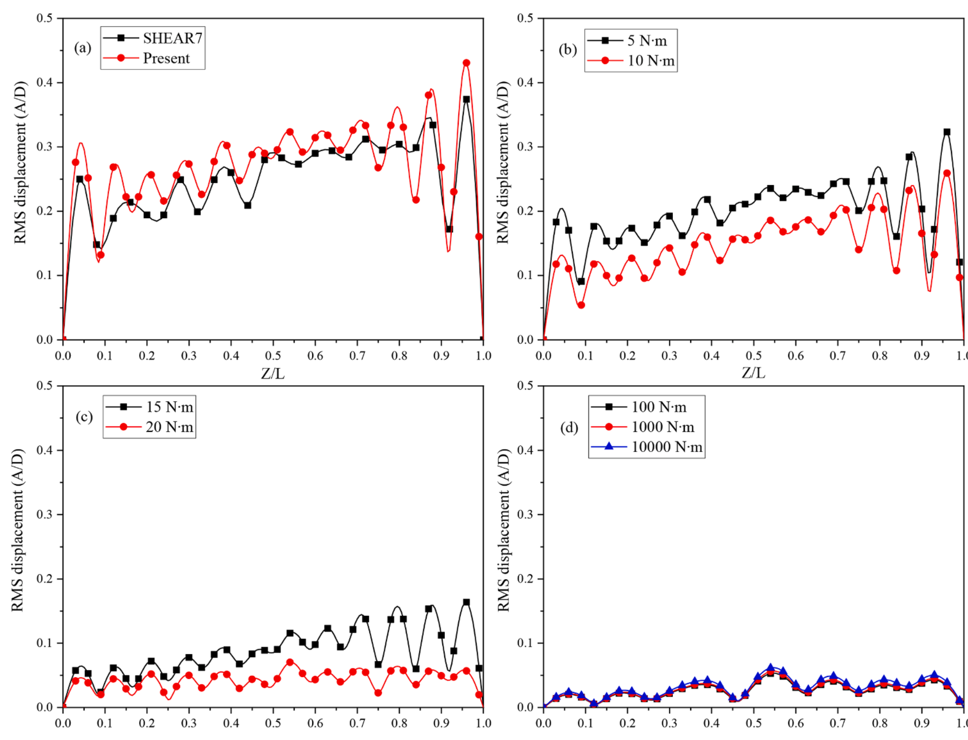

Fig. 5. Non-dimensional RMS displacement.

keeps increasing with the increase of the control bending moment. At 20 N·m, the total power ratio accounts for 73%, which is a moderate ratio and can be selected as the optimal control bending moment.

Next, the VIV of Top Tensioned Riser (TTR) will be controlled in Case three. The transverse force is simulated using the oscillating lift $F_L(z,t)$ with initial value C_{L0}=0.5, peak value C_{Lmax}=0.75, when A_{max}=0.35, and zero position A_0=1.1. S_t $=0.18.U(z)$ is a shear current. The cutoff is 0.1. The first 10 modes are selected here, i.e., n is 10. b=3, C=2.45 $\times$ $10^{11.687}$. Furthermore, the properties of the riser model are listed in Table 3 (Yu and Chen, 2019). In this section, we will show the simulation results of uncontrolled bending moment and different controlled bending moment.

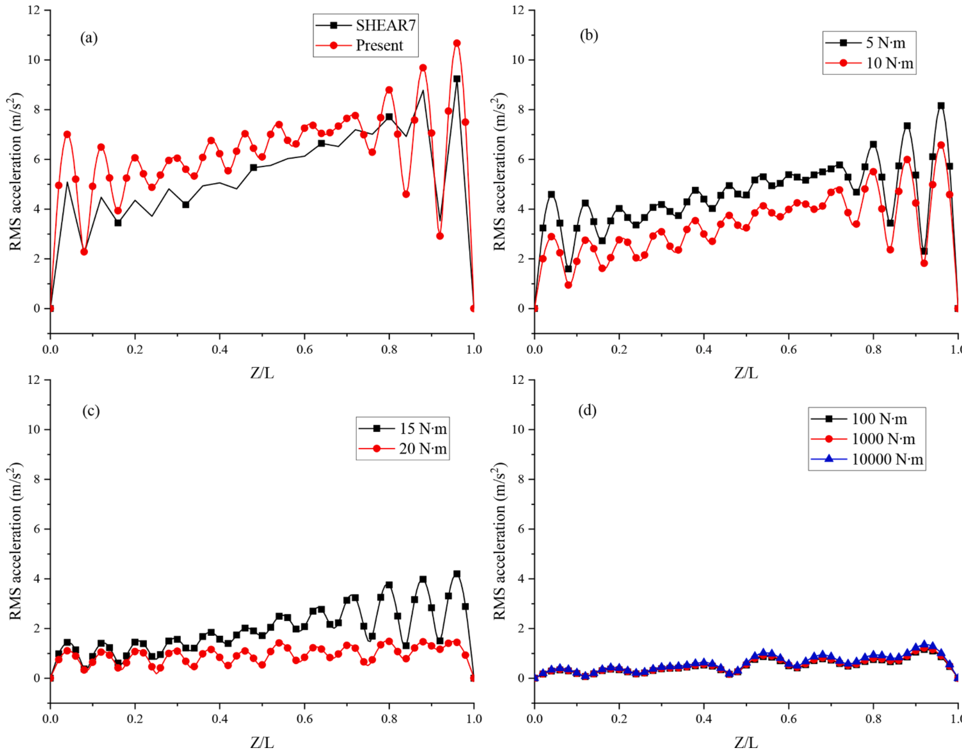

Fig. 6. RMS acceleration.

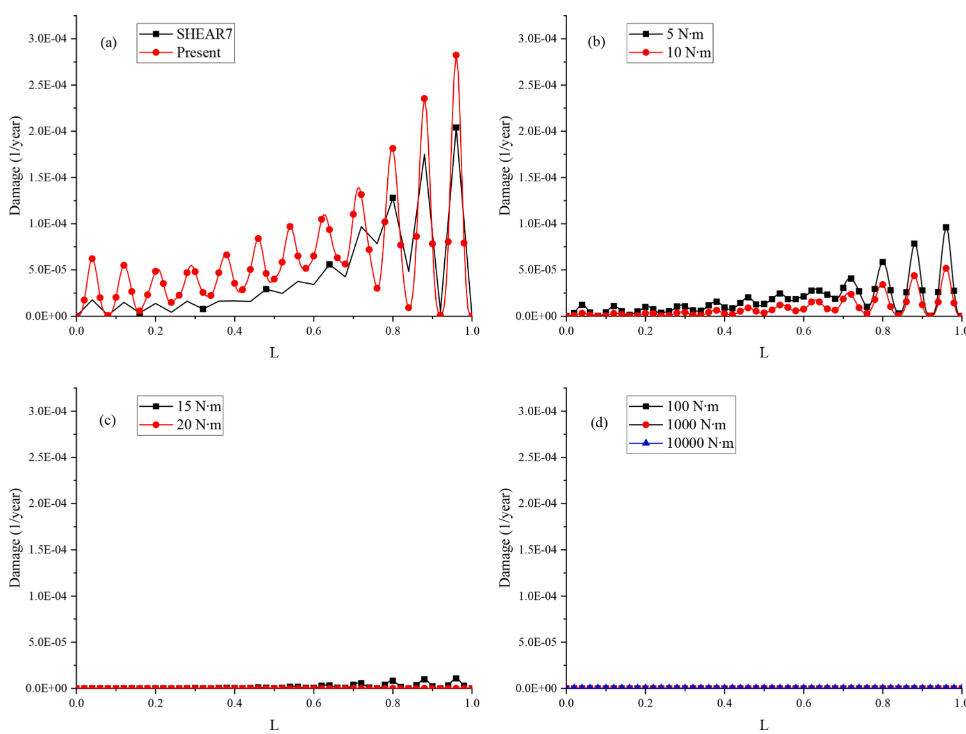

Fig. 7. Fatigue damage distributions.

The lift coefficients in bending moment input of 0 N·m, 10^3 N·m, 10^5 N·m, 10^8 N·m under shear flow(the top velocity U_{Top} is 0.5 m/s, 1.0 m/s, 1.5 m/s and 2.0 m/s, the end velocity is 0 m/s) are shown in Fig. 10. Due to the cutoff value (0.1) of the elimination mode, mode 2, mode 3 and mode 4, mode 5 and mode 6, mode 6 and mode 7 are involved in the vibration under 0.5 m/s, 1.0 m/s, 1.5 m/s and 2.0 m/s, respectively. In each excited mode, the lift coefficient distribution can be calculated by the reduced velocity of current. When two excited modal power-in region (i.e., lift coefficient distribution) have overlapping regions, power-in region overlap processing is required. When the two excited modal power-in (life force) region have no overlapping regions, there will be a gap in the lift coefficient curve. For example, Fig. 10(b), 10(c), 10(d).

The power-in region is related to the range of the reduced velocity of current in mode. So the bending moment input could not modify the

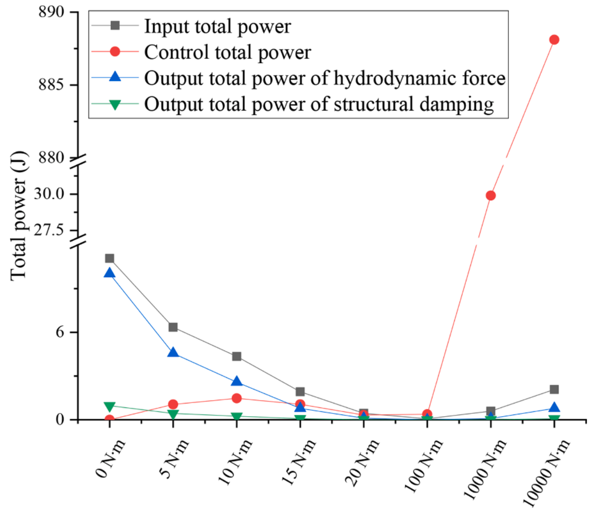

Fig. 8. Total power.

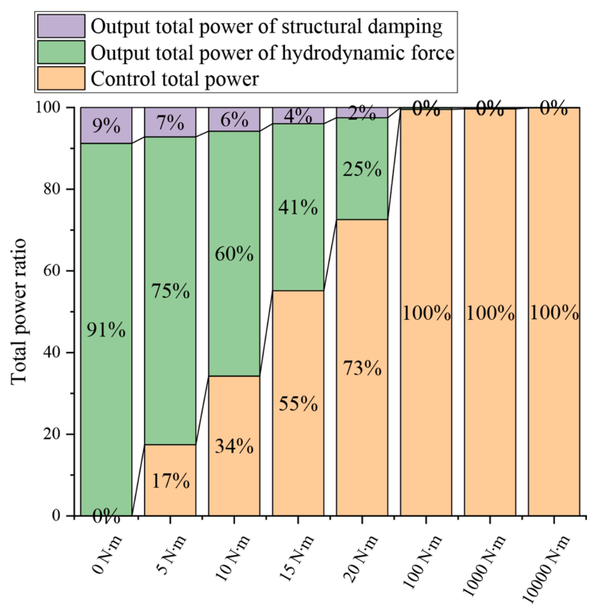

Fig. 9. Total power ratio.

Table 3
Numerical values of the system parameters.

Parameters of the physical system	Value
Length of riser(L)	1000m
Mass per unit length(m_z)	15kg/m
Outer diameter(D)	0.2m
Sea water density(ρ)	1024kg/m^3
Structural modal damping ratio(ζ_s)	0.3%
Tension(T)	1.2×10^6N
Flexural rigidity(EI)	4×10^9N·m^2
Elastic modulus(E)	2.1×10^{10}N/m^2

length of the lift force along riser, i.e., power-in region. The lift coefficients with bending moment input of 0 N·m and 10^3 N·m are almost same; the lift coefficients with 10^8 N·m are close to initial value $C_{L0} = 0.5$, which has little change in power-in region; the lift coefficients with 10^5 N·m are middle values, but at $U_{Top} = 1.5$ m/s the lift coefficients are litter larger than that with 0 N·m and 10^3 N·m. Through the above, we can obtain the conclusion that the lift coefficient can be changed only when the control bending moment is large enough. Otherwise, the lift coefficient has no change. According to Eq. (9), when the lift coefficient approaches initial value C_{L0}, the vibration amplitude A/D approaches 0. Therefore, the displacement of 10^8 N·m is smaller than that of other moment inputs.

Fig. 11 shows the Non-dimensional RMS displacement with the same moment in the same current profile. The displacement decreases as the control bending moment increases. When the control bending moment is 10^3 N·m, the displacement is the same as the uncontrolled displacement along the riser owing to the same lift coefficients. The control bending moment increases to 10^5 N·m, under $U = 0.5$ m/s or 1.0 m/s, the displacement is significantly decreased by around 68% or 40% along the riser. However, under $U = 1.5$ m/s or 2.0 m/s, the displacement is only reduced by around 4 % or 2 % along the riser. When the control bending moment is 10^8 N·m, the maximum displacement is 20 %, 26 %, 32 %, 31 % of that without control, corresponding to the velocity $U = 0.5$ m/s, 1.0 m/s, 1.5 m/s, 2.0 m/s, respectively. It can be seen that the control bending moment of 10^8N·m is better than that of 10^5 N·m in suppressing the displacement.

One important observation should be noted that the maximum displacement with the control bending moment 10^8 N·m is located at the second peak, and moves to the top of the riser with the increase of the flow velocity, while the maximum displacement with the control bending moment 10^5 N·m is located at the first peak (The peak numbers are arranged from the top to the bottom of the riser).

The fatigue damage distributions are given in Fig. 12. The fatigue value increases extremely with the increase of flow velocity, i.e., the maximum fatigue value under 2.0 m/s is around 5.1×10^5 of the value under 0.5 m/s. Compare with no control, the fatigue value with the bending moment is decrease. Under 0.5 m/s, the maximum fatigue damage with a bending moment of 10^3 N·m, 10^5 N·m, and 10^8 N·m is about 99 %, 7 %, 2 % of that without the control. When the bending moment is 10^3 N·m or 10^5 N·m, the reduced rate of maximum fatigue damage at different speeds has little difference. However, when the bending moment is 10^5 N·m, the reduced rate of the maximum fatigue damage decreases with the increase of velocity, i.e., 93 %, 74 %, 12 %, 2 %. Because the reduced rate of the displacement decreases with the increase of velocity. Moreover, under the control bending moment of 10^8 N·m, the distribution of fatigue damage shows a straight line. So the modes vibration is suppressed. The maximum fatigue damage of the control bending moment of 10^8N·m is only 2.1×10^{-2}, 5.5×10^{-2}, 3.1×10^{-2}, 5.7×10^{-2} of the maximum fatigue damage of the uncontrolled riser under 0.5 m/s, 1.0 m/s, 1.5 m/s, 2.0 m/s, respectively. It is equivalent to increasing the service life of the riser by 46, 18, 32, 17 times, respectively.

Fig. 13 shows total power ratio. As the control bending moment increases, the control total power ratio increases under different currents. When the control bending moment is unchanged, the control total power ratio decreases with the increase of the currents. For example, when the bending moment is 10^5 N·m, the total energy ratio is 73%, 43%, 14%, 10% at 0.5m/s, 1.0m/s, 1.5m/s, and 2m/s, respectively. In other words, the greater the shear currents, the greater the control bending moment required. By comparing the control total power ratio, it is found that the control bending moment is 10^3 N·m too small, the control bending moment is 10^8 N·m too large, and 10^5 N·m is moderate.

5. Conclusion

The boundary control method in frequency domain is studied to control the vortex induced vibration of riser in shear flow. A semi-empirical control approach is developed based on input and output power are in balance in one mode. The numerical results show that this proposed approach can effectively control the response level of riser VIV under shear flow. The conclusions obtained can be summarized as follows:

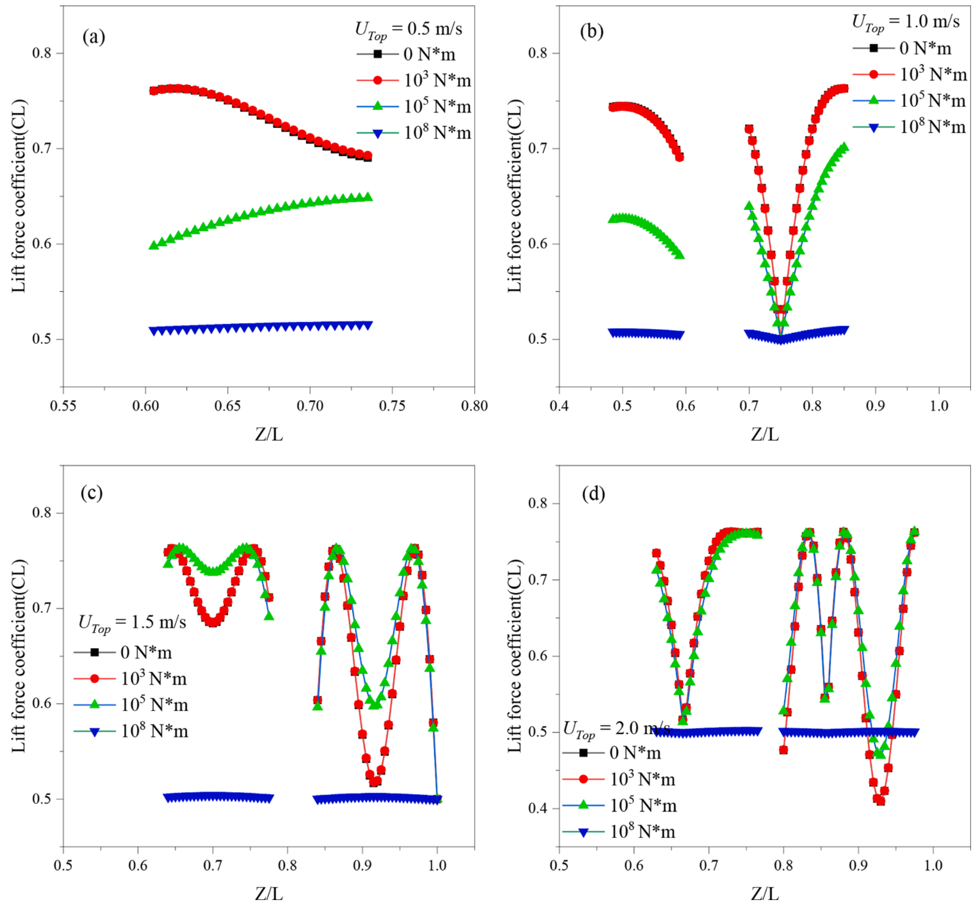

Fig. 10. Lift force coefficient.

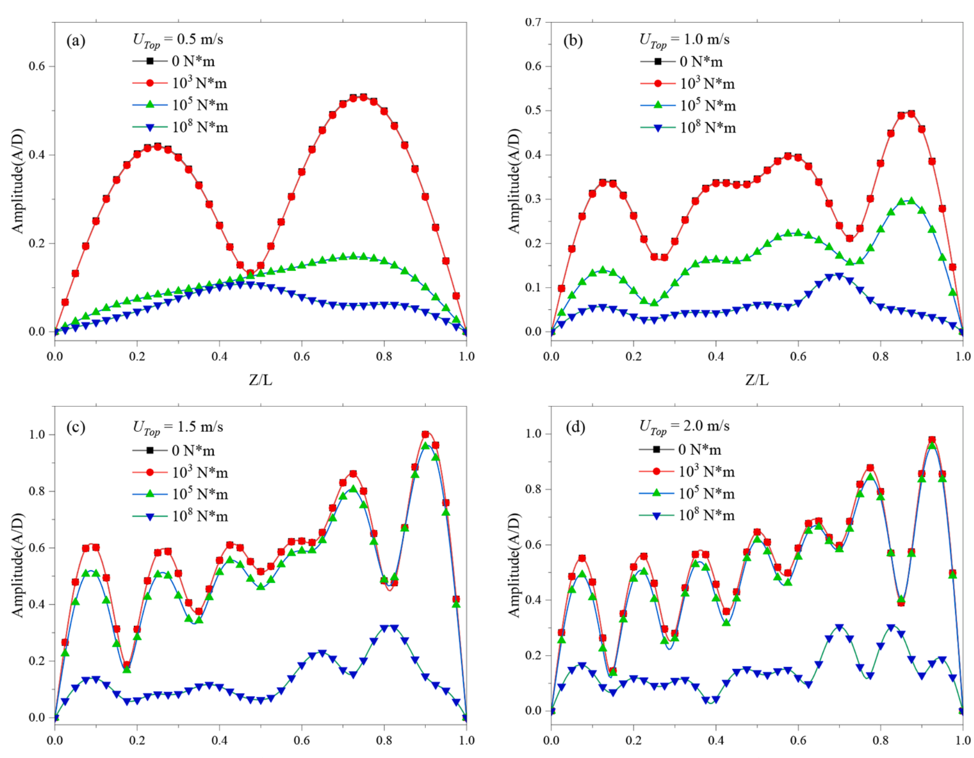

Fig. 11. Non-dimensional RMS displacement.

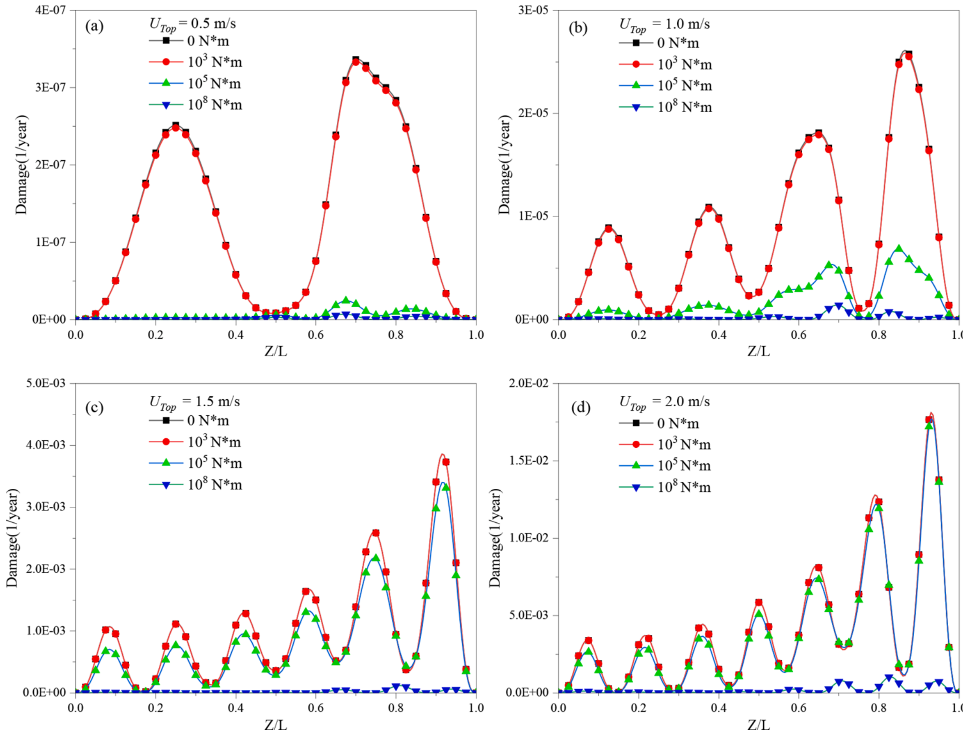

Fig. 12. Fatigue damage distributions.

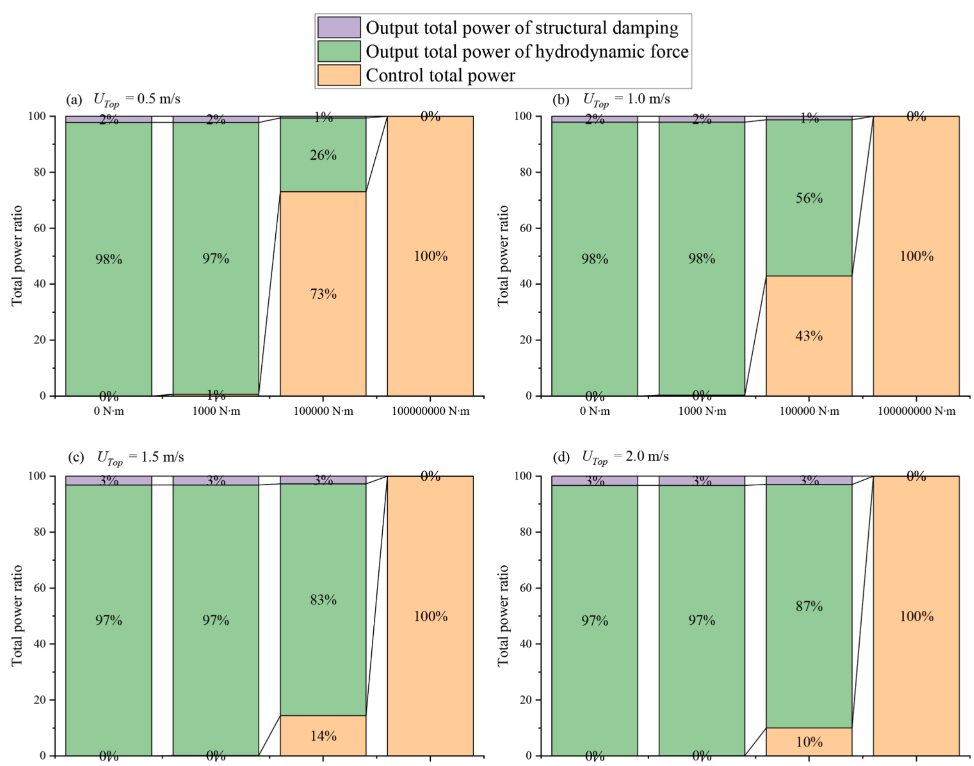

Fig. 13. Total power ratio.

1 The control bending moment at the same frequency as the riser's VIV can effectively suppress the riser's VIV without wasting input energy due to the phase difference. Moreover, simple sinusoidal bending moment control is easy to implement in engineering.
2 The vibration control bending moment is inversely proportional to the displacement. The displacement decreases with the increase of bending moment control. However, the displacement reduction of the riser becames smaller when the bending moment exceeds the critical value. In case two of 100 N·m, 1000 N·m, and 10000 N·m, the displacements almost coincide. It shows that with the increase of the bending moment, the vibration displacement of the riser gradually decreases, approaching the minimum value, but not zero.

3 There is an inverse proportional relationship between the vibration control bending moment of the riser and the fatigue damage of the riser. As the bending moment control increases, the fatigue damage of the riser decreases. However, when the bending moment exceeds the critical value, the fatigue of the riser will no longer decrease. In last case, the maximum fatigue damage of 10^8 N·m control bending moment is only 2.1×10^{-2}, 5.5×10^{-2}, 3.1×10^{-2}, 5.7×10^{-2} of the maximum fatigue damage of the uncontrolled riser under 0.5m/s, 1.0m/s, 1.5m/s, 2.0m/s, respectively. It is equivalent to increasing the service life of the riser by 46, 18, 32, 17 times, respectively. Moreover, the control bending moment is not the optimal bending moment. How to obtain the optimal control bending moment is the next step worthy of research.
4 The value of control bending moment is discussed from the point of view of total power. The larger the control moment is, the larger the control energy is, and the smaller the displacement and fatigue damage of the riser is. However, when the total output power is much greater than the total input power and the dynamic response of the structure is controlled by the control bending moment, the displacement and fatigue damage of the riser will not be reduced. This is excessive control and should be avoided. For example, when the control bending moment is more significant than 100 N·m, the output total power is much higher than the input total power in case two. When the control bending moment is unchanged, the control total power ratio decreases with the increase of the currents. In last case, when the bending moment is 10^5 N·m, the total energy ratio is 73%, 43%, 14%, 10% at 0.5m/s, 1.0m/s, 1.5m/s, and 2m/s, respectively. In other words, the greater the shear currents, the greater the control bending moment required.

Declaration of Competing Interest

The authors declare that they have no conflict of interest.

The authors declare that they have no known competing financial interests or personal relationships that could have appeared to influence the work reported in this paper.

Acknowledgments

This work is supported by the Strategic Priority Research Program of the Chinese Academy of Sciences (Grant No. XDA22000000).

References

Liu, G, Li, H, Qiu, Z, Leng, D, Li, Z, Li, W, 2020. A mini review of recent progress on vortex-induced vibrations of marine risers. Ocean Eng. 195, 106704.
Thorsen, MJ, Challabotla, NR, Sævik, S, Nydal, OJ, 2019. A numerical study on vortex-induced vibrations and the effect of slurry density variations on fatigue of ocean mining risers. Ocean Eng. 174, 1–13.
Iranpour, M, Taheri, F, Vandiver, JK, 2008. Structural life assessment of oil and gas risers under vortex-induced vibration. Mar. struct. 21, 353–373.
Wu, X, Ge, F, Hong, Y., 2012. A review of recent studies on vortex-induced vibrations of long slender cylinders. J. Fluids Struct. 28, 292–308.
Ren, H, Xu, Y, Cheng, J, Cao, P, Zhang, M, Fu, S, et al., 2019. Vortex-induced vibration of flexible pipe fitted with helical strakes in oscillatory flow. Ocean Eng. 189, 106274.
How, BVE, Ge, SS, Choo, YS, 2009. Active control of flexible marine risers. J. Sound Vib. 320, 758–776.
Do, KD, Pan, J, 2008. Boundary control of transverse motion of marine risers with actuator dynamics. J. Sound Vib. 318, 768–791.
Do, KD, Pan, J, 2009. Boundary control of three-dimensional inextensible marine risers. J. Sound Vib. 327, 299–321.
Ge, SS, He, W, How, BVE, Choo, YS, 2010. Boundary Control of a Coupled Nonlinear Flexible Marine Riser 18, 1080–1091.
Zhao, Z, Liu, Z, Li, Z, Wang, N, Yang, J, 2017. Control design for a vibrating flexible marine riser system. J. Franklin Inst. B 354, 8117–8133.
He, W, Ge, SS, How, BVE, Choo, YS, Hong, K-S, 2011. Robust adaptive boundary control of a flexible marine riser with vessel dynamics. Automatica 47, 722–732.
Liu, Y, Guo, F, 2017. Output feedback boundary control of a flexible marine riser system. J. Vib. Control 24, 3617–3630.
Zhao, Z, Ahn, CK, Wen, G, 2019. Cooperative disturbance rejection control of vibrating flexible riser systems. Nonlinear Dyn. 98, 1603–1613.
Guo, F, Liu, Y, Luo, F, Wu, Y, 2019. Vibration suppression and output constraint of a variable length drilling riser system. J. Franklin Inst. 356, 1177–1195.
Shaharuddin, NMR, Darus, IZM, 2012. Active vibration control of marine riser. In: Control, Systems & Industrial Informatics (ICCSII), 2012 IEEE Conference on.
Zhang, W-S, Li, D-D, 2015. Active control of axial dynamic response of deepwater risers with Linear Quadratic Gaussian controllers. Ocean Eng. 109, 320–329.
Quen, LK, Tang, CH, Kang, H, Gang, M, 2016. Neural-network prediction of riser top tension for vortex induced vibration suppression. In: 2016 IEEE International Conference on Underwater System Technology: Theory and Applications (USYS), pp. 1–6.
Ji, N, Liu, Z,, Liu, J and, 2018. He W, Vibration control for a nonlinear three-dimensional Euler–Bernoulli beam under input magnitude and rate constraints. Nonlinear Dyn. 91, 2551–2570.
Yu J and Chen W. Active Control of Flexible Riser Vibration by Boundary Control Based on LQR Controller. 2019.
Pham, P-T, Hong, K-S, 2019. Vibration control of a flexible marine riser with time-varying length. In: 2019 12th Asian Control Conference (ASCC): IEEE, pp. 778–783.
Hasheminejad, SM, Rabiee, AH, Jarrahi, M, Markazi, AHD, 2014. Active vortex-induced vibration control of a circular cylinder at low Reynolds numbers using an adaptive fuzzy sliding mode controller. J. Fluids Struct. 50, 49–65.
Tavasoli, A, 2015. Adaptive robust boundary control of shaft vibrations under perturbations with unknown upper bounds. Int. J. Adapt. Control Signal Process. 29, 537–562.
He, W, Meng, T, 2018. Adaptive Control of a Flexible String System With Input Hysteresis. IEEE Trans. Control Syst. Technol. 26, 693–700.
He, X, Zhao, Z, Su, J, Yang, Q, Zhu, D, 2019. Adaptive inverse control of a vibrating coupled vessel-riser system with input backlash. IEEE Trans. Syst. Man Cybern.
Zhao, Z, Ahn, CK, Li, H-X, 2020. Dead zone compensation and adaptive vibration control of uncertain spatial flexible riser systems. IEEE/ASME Trans. Mechatron. 25, 1398–1408.
Hong, K-S, Shah, UH, 2018. Vortex-induced vibrations and control of marine risers: a review. Ocean Eng. 152, 300–315.
Li, Y, Guo, S, Chen, W, 2018. Analysis on multi-frequency vortex-induced vibration and mode competition of flexible deep-ocean riser in sheared fluid fields. J. Pet. Sci. Eng.
Blevins, R., 1977. Flow-induced Vibration.
Faltinsen, OM, 1990. Sea Loads on Ships and Offshore Structures. Cambridge University Press, New York.
Weaver, W, Timoshenko, S, Young, D, 1990. Vibration Problems in Engineering. Wiley, New York.
Vandiver JKand Li L, SHEAR7 V4.4 Program Theoretical Manual. 2005.
Oakley, O., Marcollo, H., Tognarelli, M., Triantafyllou, M., Mukundan, H., Zheng, H., 2007. Vortex Induced Vibration Data Repository. Center for Ocean Engineering, MIT, 2007 ed.
Vandiver, JK, 2012. Shear7. MIT: MIT, 11, p. 10.